



Geometrical and distributed surface barriers in $\text{Bi}_2\text{Sr}_2\text{CaCu}_2\text{O}_8$

N. Morozov^{a,b,*}, E. Zeldov^a, M. Konczykowski^b, R.A. Doyle^c

^a Department of Condensed Matter Physics, The Weizmann Institute of Science, 76100 Rehovot, Israel

^b CNRS, URA 1380, Laboratoire des Solides Irradiés, Ecole Polytechnique, 91128 Palaiseau, France

^c Interdisciplinary Research Center in Superconductivity, University of Cambridge, West Cambridge Site, Cambridge CB3 0HE, UK

Received 13 June 1997; accepted 19 August 1997

Abstract

The local ac magnetic response in $\text{Bi}_2\text{Sr}_2\text{CaCu}_2\text{O}_8$ crystals of platelet and prism shapes has been measured using microscopic arrays of Hall sensors. At elevated temperatures the ac response in platelet samples is governed by the geometrical barrier whereas a distributed Bean–Livingston surface barrier is dominant for the prism-shaped sample. In the local measurements these two barriers display qualitatively different behavior and can be individually studied. Models for the local ac response are derived for the two cases and good agreement with experiment is obtained. © 1997 Elsevier Science B.V.

PACS: 74.60.Ec; 74.60.Ge; 74.60.Jg; 74.62.Hs

Keywords: Vortex dynamics; Surface barrier; Geometry effect; Magnetic susceptibility

1. Introduction

Magnetic hysteresis and irreversibility are among the most commonly investigated properties of high-temperature superconductors (HTSC). Hysteretic behavior is readily measured using either dc or ac experimental techniques. It provides valuable information on vortex dynamics and pinning which are of central importance for both fundamental and applied research [1–3]. The common source of hysteresis in superconductors is bulk vortex pinning due to material defects and inhomogeneities [1–5]. However, there are at least two additional important mechanisms of magnetic irreversibility, the Bean–Livingston (BL) surface barrier [6–17] and the geometrical barrier [18–25] [26–35]. The BL surface barrier is the result of a competition between two forces, the image force that attracts a vortex towards a parallel surface, and the Lorentz force due to Meissner shielding currents that drives vortices into the bulk of the sample. The geometrical barrier arises due to a competition between the elongation energy of a vortex penetrating into the sample corners and the Lorentz force. Because they have different physical origins, these two barriers depend differently on experimental conditions. The

* Corresponding author. Present address: Superconductivity Technology Center, Los Alamos National Laboratory, K763, Los Alamos, NM 87545. Tel.: +1 505 667 3656; fax: 1 505 665 3164; e-mail: morozov@lanl.gov

geometrical barrier is determined by the shape of the sample, whereas the BL barrier is sensitive to surface quality as well as thermal relaxation processes. Usually in low pinning HTSC all three mechanisms affect the vortex behavior. It is therefore difficult to distinguish between the various contributions to the magnetic hysteresis using global magnetization experiments without complicated modeling [35,36]. Although it has recently been claimed that BL surface barriers in HTSC are irrelevant due to the poor surface quality and sharp corners [37,38], we present compelling evidence here that the surface barrier may play a dominant role in magnetic hysteresis in low pinning samples of HTSC.

In this paper we show that both geometrical and surface barriers are important in HTSC and their individual contributions can be studied separately by proper shaping of the samples. We investigate the local ac response in $\text{Bi}_2\text{Sr}_2\text{CaCu}_2\text{O}_8$ (BSCCO) crystals at elevated temperatures where bulk pinning is negligible and the magnetic response is governed predominantly by the surface and geometrical barriers. In platelet-shaped samples in perpendicular applied field direct separation between the geometrical and surface barriers is difficult, even with local techniques [28,29]. The geometrical barrier can however be suppressed by changing the shape of the crystals. In particular, a prism geometry has no geometrical barrier [39]. In this configuration, however, the BL surface barriers become distributed over the entire surface of the sample and have a more pronounced effect [40]. In the following sections the ac response in platelet and prism geometries is derived and compared with the experimental results. It is shown that the local responses in these two cases are strikingly different reflecting the distinct underlying irreversibility mechanisms.

2. Experimental technique

The local ac susceptibility has been measured on several high quality BSCCO single crystals. The crystals with $T_c \approx 90$ K were grown using a traveling solvent floating zone method [41]. Three samples were cut from one large crystal. Samples A and B were $110 \times 240 \times 25 \mu\text{m}^3$ and $240 \times 300 \times 40 \mu\text{m}^3$ respectively, and sample C was polished into a triangular prism shape with base $660 \times 270 \mu\text{m}^2$ and a height of $70 \mu\text{m}$ along the c -axis.

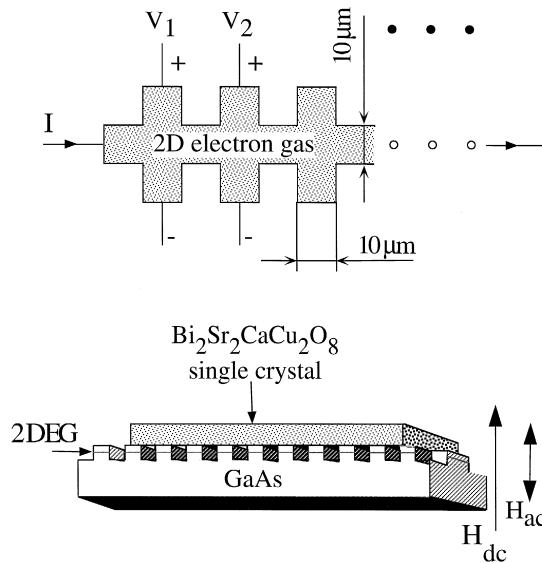


Fig. 1. The array of GaAs Hall sensors. Schematic layout of the photolithographically patterned two-dimensional electron-gas active layer (top), and the experimental setup (bottom). Both dc and ac magnetic fields are applied along the c -axis of the sample.

The samples were placed on the surface of an array of micro Hall sensors fabricated from a GaAs/AlGaAs heterostructure [29] (see Fig. 1). Crystal A was studied using an array of 10 sensors with active areas of $3 \times 3 \mu\text{m}^2$. For the other samples, $10 \times 10 \mu\text{m}^2$ sensors were used. These sensors combine extremely high sensitivity (of about $0.1 \Omega/\text{G}$) with high spatial resolution. The dc and ac magnetic fields were applied along the c -axis of the crystals. The samples were cooled in zero applied field and then the local ac response was measured as a function of dc magnetic field at constant temperature. The ac component of the Hall voltage was detected using a standard lock-in technique. Both components of the ac magnetic response were measured for each of the sensors across the sample: the in-phase component B'_{ac} describing the shielding, and the out-of-phase component B''_{ac} related to the ac losses. The experiment allowed simultaneous measurement of both dc and ac responses. All experiments were carried out at low frequency. There was practically no frequency dependence of ac response in the range of 10–100 Hz at elevated temperatures and all presented results were obtained at $f = 37$ Hz.

3. Platelet geometry

3.1. Equilibrium magnetization

We start by considering a long platelet sample of width $2W$ ($-W < x < W$) and thickness $d \ll W$, ($-d/2 < z < d/2$) with no bulk pinning in the presence of a transverse applied field $H_a \parallel z$ (see Fig. 2). The magnetization process is described as follows. At low applied fields the induced Meissner currents shield the interior of the sample and no vortices are present except in the sharp corners at $|x| \approx W$ and $|z| \approx d/2$ as shown in Fig. 2(a). As the field increases the curved vortices cutting through the corners elongate until they merge at $z = 0$.

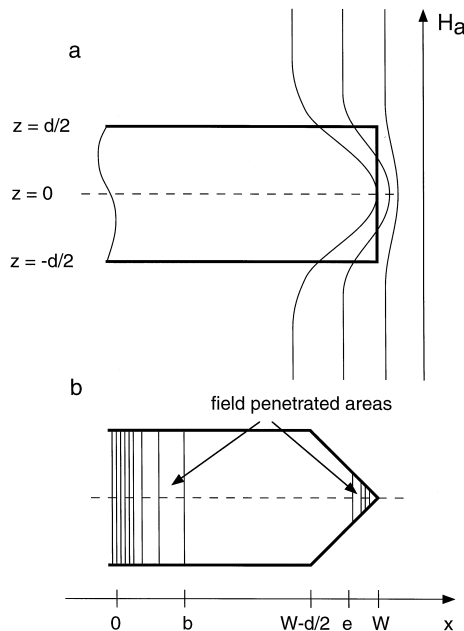


Fig. 2. Platelet sample in transverse magnetic field. (a) The curved vortices penetrate into the corners of the sample with increasing applied field until they merge at $z = 0$. (b) Field penetration in the model tapered edge of the sample. Straight vortices fill the edge region $e < x < W$. At $H_{dc} > H_p$ a central vortex droplet of width $2b$ is formed.

$z = 0$ when the field reaches the value of the penetration field H_p . If the field is further increased the vortices are driven by the Meissner current to the center of the sample at $x = 0$.

In order to simplify the mathematical description of the geometrical barrier we model this process by describing the edge region as a tapered edge at $W - d/2 < |x| < W$ with angle $2\alpha = 90^\circ$ filled by straight vortices at $e < |x| < W$ as shown in Fig. 2(b). The energy of the vortex is given by its line energy $\epsilon_0 = \phi_0 H_{c1}/4\pi$ times the length of the vortex, which grows linearly and then saturates for $|x| < W - d/2$. Let us consider a vortex in the edge region of the sample (Fig. 2(b)). A shift of this vortex by Δx into the sample will increase the vortex energy due to its elongation $\Delta z = 2\Delta x \tan \alpha = 2\Delta x$ by $\Delta U = 2\Delta x \epsilon_0$. As a result there is a horizontal force F_{lt} in the tapered part of the sample due to the vortex line tension. This drives the vortex towards the sample edge. The other force acting on the vortex is a Lorentz force, $F_L = J_y(x)\phi_0/c$ due to interaction of the vortex with the Meissner current $J_y(x)$. This force acts towards the sample center. In the steady state situation these two forces, acting in opposite directions, have to be balanced by setting an appropriate value of $J_y(x)$ in the edge region. As the field increases the vortex-filled region $e < |x| < W$ at the edge of the sample expands until the flux front e reaches $x = W - d/2$ at $H_a = H_p$. Beyond this point the x -component of the line-tension force disappears ($F_{lt} = 0$) and the Lorentz force drives the penetrating vortices towards the sample center. At fields above H_p the penetrated vortices are focused by the surrounding Meissner currents in the center of the sample, forming a droplet of vortices.

The dc magnetic field and current distributions in platelet samples in the presence of a geometrical barrier were recently derived in detail in Refs. [18,19,32,33]. The following analytical expression is obtained, in the zero-pinning case, for the distribution of the magnetic induction across the sample

$$B_z(x) = \frac{2H_{c1}}{\pi} \ln \frac{\sqrt{|e^2 - x^2|(W^2 - b^2)} + \sqrt{|b^2 - x^2|(W^2 - e^2)}}{\sqrt{(e^2 - b^2)|W^2 - x^2|}} \quad |x| < b \text{ or } |x| > e, \quad (1)$$

$$B_z(x) = 0 \quad b < |x| < e.$$

where b and e are two spatial parameters describing the half width of vortex droplet in the center of the sample and the width of the edge field penetrated region (Fig. 2(b)), and x is the distance from the center of the sample. The parameters b and e are determined by the magnetization history and by the applied field

$$H_a = \frac{2H_{c1}}{\pi} \ln \frac{\sqrt{W^2 - b^2} + \sqrt{W^2 - e^2}}{\sqrt{e^2 - b^2}}. \quad (2)$$

The global magnetization due to the geometrical barrier is then given by

$$M = -\frac{H_{c1}}{4\pi Wd} \sqrt{(W^2 - b^2)(W^2 - e^2)}. \quad (3)$$

Fig. 3 describes the corresponding hysteretic magnetization loop (solid line). After zero field cooling $H_a = 0$ and the parameters $e = W$ and $b = 0$. As H_a is increased the vortices first penetrate only into the sample edges and parameter e decreases while b initially remains zero. At $H_a = H_p$ the parameter e reaches its minimum value $e_{\min} \approx W - d/2$ and the first vortex overcomes the geometrical barrier and enters into the bulk of the sample. The corresponding field is $H_p \approx (2H_{c1}/\pi)\sqrt{d/W}$. Above this field vortices penetrate into the center of the sample, and b increases approaching its maximum value $b_{\max} \approx W - d/2$ with constant $e = e_{\min}$. The magnetization for the increasing field branch of the dc magnetization loop in Fig. 3 is given by

$$M_{\text{inc}} = -\frac{H_{c1}}{4\pi} \coth\left(\frac{\pi H_a}{2H_{c1}}\right) \approx -\frac{H_{c1}}{4\pi\sqrt{Wd}} \sqrt{W^2 - b^2}. \quad (4)$$

On the decreasing field, (for $H > 0$) the vortices are trapped in the bulk of the sample by the Meissner current (see Fig. 4). As the field decreases, the vortex droplet first expands up to a maximum allowed value

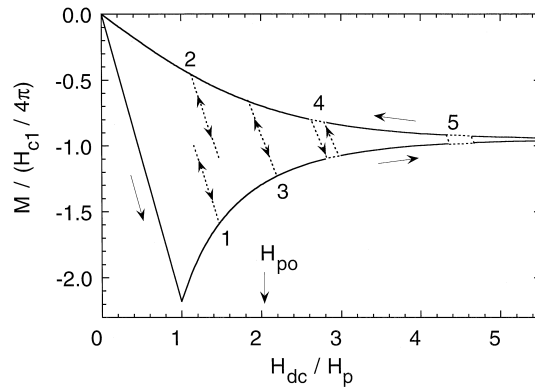


Fig. 3. The theoretical dc magnetization loop due to geometrical barrier (solid) and ac magnetization trajectories at various positions along the loop (dashed) ($d/W = 0.2$, $H_{ac} = 0.17H_p$).

$b_{max} = W - d/2$, and only then the vortices begin to leave the sample. The parameter e increases with the decreasing field and approaches W at $H_a = 0$. On the decreasing branch of Fig. 3, the global magnetization is given by

$$M_{dec} = -\frac{H_{c1}}{4\pi} \tanh\left(\frac{\pi H_a}{2H_{c1}}\right) \approx -\frac{H_{c1}}{4\pi\sqrt{Wd}} \sqrt{W^2 - e^2}. \quad (5)$$

The hysteretic magnetization due to the geometrical barrier becomes reversible at fields on the order of H_{c1} .

In the presence of a BL surface barrier in addition to the geometrical barrier the above description is modified only slightly. As described in detail in Section 4 below, the decreasing field branch of the magnetization loop is practically unchanged since there is no effective BL surface barrier for vortex exit. On increasing field however, the magnetization can be enhanced significantly by the additional barrier in the tapered edge region. In this case M will be given by the same expressions as above with H_{c1} replaced by some higher characteristic field of the BL surface barrier. As a result the hysteresis will be larger and the irreversibility field may become significantly higher than H_{c1} . The qualitative behavior nevertheless remains similar to the case of the geometrical barrier.

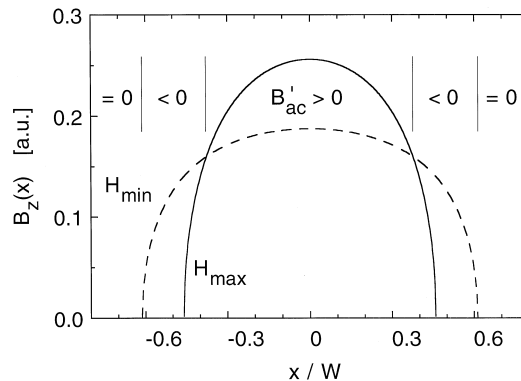


Fig. 4. Dome shaped field profile $B_z(x)$ at H_{max} (solid) and H_{min} (dashed) following Eq. (1). In the center of the vortex droplet the ac response B'_{ac} is always positive. Near the edges of the vortex droplet B'_{ac} attains negative values. In the vortex-free regions $B'_{ac} = 0$.

3.2. The local ac response for a platelet-shaped sample

The local ac response in the platelet sample exhibits rather unusual behavior due to the geometrical barrier. Let us first consider the expected susceptibility χ' for a small ac field with amplitude $H_{ac} \ll H_p$. The total instantaneous applied field is given by $H_a(t) = H_{dc} + H_{ac} \cos(\omega t)$. We define a local permeability $\mu(x) = \mu' - i\mu'' = (B'_{ac} - iB''_{ac})/H_{ac}$ where $B'_{ac}(x)$ and $B''_{ac}(x)$ are the in-phase and out-of-phase amplitudes of ac components of the local field $B_z(x)$ measured at the fundamental frequency. The real part of the local susceptibility $\chi' = (1/4\pi)(\mu' - 1)$ is expected to be $-1/4\pi$ in the Meissner state, gradually increasing monotonically to zero in the fully penetrated state. This behavior is indeed commonly observed in global measurements [35]. In the case of local measurements however, the behavior is much richer and more complicated [31].

A remarkable phenomenon takes place at fields slightly above H_p . The number of vortices in the sample is determined by the peak field value, $H_a^{\max} = H_{dc} + H_{ac}$. The corresponding field profile is shown by the solid line in Fig. 4. When the instantaneous magnetic field decreases, the Meissner current and the associated Lorentz force which acts to focus vortices in the center of the sample also decrease. As a result the vortex droplet starts to spread out (both parameters b and e increase). Provided the condition $b < W - d/2$ is held, however, vortices cannot leave the sample, and the ‘‘captured’’ flux $\Phi = \int_{-b}^b B_z(x) dx$ is constant. If H_{ac} and H_{dc} are small enough, this condition will still be satisfied at the minimum instantaneous field $H_a^{\min} = H_{dc} - H_{ac}$. The new field distribution calculated under this constraint is plotted as the dashed line in Fig. 4. On increasing instantaneous applied field the vortex droplet is compressed again. Thus the vortex droplet ‘‘breathes’’ with the ac field and the edges of the vortex droplet ($|x| = b$) move in opposite phase with respect of the instantaneous field $H_a(t)$.

In Fig. 5 we present numerical simulations of the local ac response calculated using static Eqs. (1) and (2) above as a function of H_{dc} for different positions across the sample. In the sample center $B_z(x)$ increases with

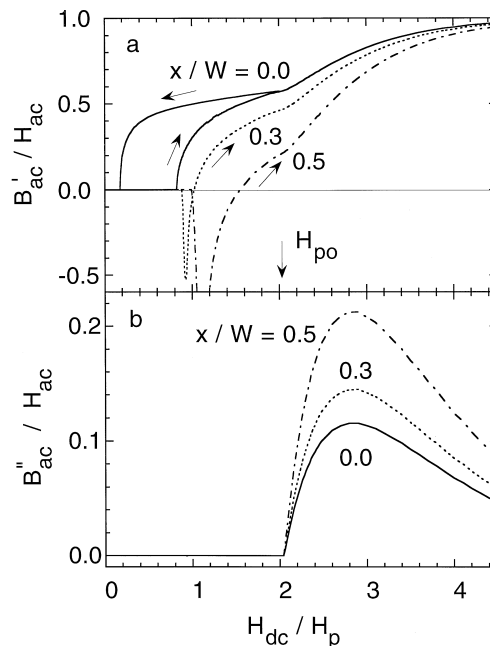


Fig. 5. Calculated local ac response B'_{ac} (a) and B''_{ac} (b) due to geometrical barrier in platelet sample at various locations x/W across the sample as a function of H_{dc} . A negative B'_{ac} appears in the vicinity of H_p for $|x|/W > 0$. The dissipation signal B''_{ac} appears at H_{po} and is accompanied by a kink in B'_{ac} . B'_{ac} is hysteretic at $H_{dc} < H_{po}$ (shown only for $x = 0$).

H_a and hence the local permeability is positive. However, close to the droplet edges $B_z(x)$ decreases with increasing instantaneous $H_a(t)$ and therefore $B'_{ac}(x)$ is in anti-phase with H_{ac} resulting in a negative local μ' and B'_{ac} which is clearly demonstrated in the Fig. 5(a). A negative value for B'_{ac} is in striking contrast to the predictions of all the common ac susceptibility models [5,42–49] which predict a positive B'_{ac} everywhere in the bulk of the sample. The main source of the discrepancy is that in the standard models vortices penetrate and leave the sample during each cycle of the ac field. In our case however the geometrical barrier enforces an invariant number of vortices inside the sample. Therefore the vortex droplet undergoes only compressional deformations that result in positive μ' in the center and negative μ' closer to the edges. Note that the global μ' of the entire sample is always positive and this unique negative response can be observed only by use of local measurements.

Now we consider χ'' . We showed above that for small ac fields, the number of vortices in the sample is preserved during an ac cycle. In our quasistatic approach the ac measurements are equivalent to determination of minor loops on a magnetization loop as shown Fig. 3 (dashed lines). In the absence of bulk pinning and at low fields, these trajectories are reversible which results in $\chi'' = 0$ (Fig. 5(b)). As H_{dc} increases, the width of the dc magnetization loop decreases, and at some point the amplitude of H_{ac} becomes sufficient to cross between the ascending and descending branches of the dc loop as shown by trajectory 3 in Fig. 3. We denote the dc field at this point as the pinch-off field, H_{po} . For $H_{dc} > H_{po}$ the minor magnetization loop due to the ac field becomes hysteretic and dissipation thus appears. The global dissipation is proportional to the area enclosed by the minor loops. It reaches a sharp maximum at point 4 in Fig. 3. The pinch-off field H_{po} is determined by the shape of the magnetization loop (i.e., by sample geometry and by H_{c1}) and H_{ac} , and is independent of the observation point x in the crystal. The amplitude of the out-of-phase component of the ac response, however, is strongly position dependent, increasing from the center towards the sample edge (Fig. 5(b)). Note that the maximum dissipation appears at the same field everywhere in the sample. This maximum is the same as that normally observed by global measurements and sometimes erroneously attributed to the bulk pinning properties of the sample. At higher fields the dissipation decreases again as hysteresis in the full magnetization loop shrinks and then vanishes (point 5 in Fig. 3).

The origin of the dissipation is the following. The dissipative signal appears when the vortex droplet reaches the sample edges and vortices leave and enter the crystal during each ac cycle. There is little or no dissipation otherwise since there is no bulk pinning. The geometrical barrier is asymmetric with respect to vortex entry and exit. As a result on increasing field vortices enter the sample with a high potential energy in order to overcome the barrier, and leave the sample on decreasing field at low potential. The observed dissipation signal is due to the work carried out by the external field against the geometrical barrier. This mechanism is fundamentally different from the dissipation due to bulk pinning and results in the unique local response as shown in Fig. 5.

3.3. Experimental results

Fig. 6 shows experimentally determined B'_{ac} at $T = 77.5$ K in platelet BSCCO crystal as a function of H_{dc} measured by 10 μm Hall sensors. At $x = 0$ a positive B'_{ac} appears with the formation of the vortex droplet at $H_{dc} = H_p - H_{ac}$. Away from the center, however, $B'_{ac} = 0$ as long as the size of the droplet is small. As H_{dc} increases the droplet edge b reaches the observation point x resulting in a negative B'_{ac} that gradually turns positive with any further increase of H_{dc} . The negative B'_{ac} occurs at progressively higher H_{dc} at larger x/W . This data was obtained with a large ac modulation ($H_{ac} = 5$ G rms) which slightly smears the sharp theoretical peaks.

Fig. 7 presents the experimental B'_{ac} and B''_{ac} as a function of H_{dc} for different positions across the sample. In addition to the negative dip in B'_{ac} and the dissipation peak which have been discussed above, three distinct features are predicted at H_{po} : a sharp onset of B'_{ac} , a kink in B'_{ac} , and a hysteretic B'_{ac} at $H_{dc} < H_{po}$ [31]. Further, as suggested above, the experimental $B'_{ac}(x)$ is largest at $x = 0$, while $B''_{ac}(x)$ is highest close to the

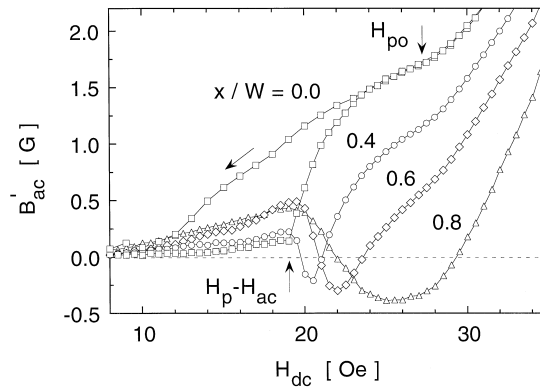


Fig. 6. Experimental B'_{ac} in BSCCO platelet crystal as a function of H_{dc} measured using $10\ \mu\text{m}$ sensors at various locations x/W across the sample ($T = 77.5\ \text{K}$, $H_{ac} = 5\ \text{G rms}$). For clarity, the ac response is shown for the decreasing applied field only at the center of the sample.

edges in accord with the model. In addition, the dissipation peaks are asymmetric with a slower fall-off at the high-field side. All these features are clearly experimentally resolved in Figs. 6 and 7.

An interesting observation is the hysteresis in local B'_{ac} as a function of H_{dc} at low fields as shown in Fig. 5(a) and Fig. 6 (presented only for $x=0$ for clarity). This hysteresis is another characteristic feature of the geometrical barrier that is not obtained in other models. On the decreasing branch of the dc magnetization loop the vortex droplet extends to the sample edges [18,19]. The deformation of the dome by H_{ac} results in negative B'_{ac} only close to the sample edges, whereas the rest of the sample displays a positive B'_{ac} that is larger on

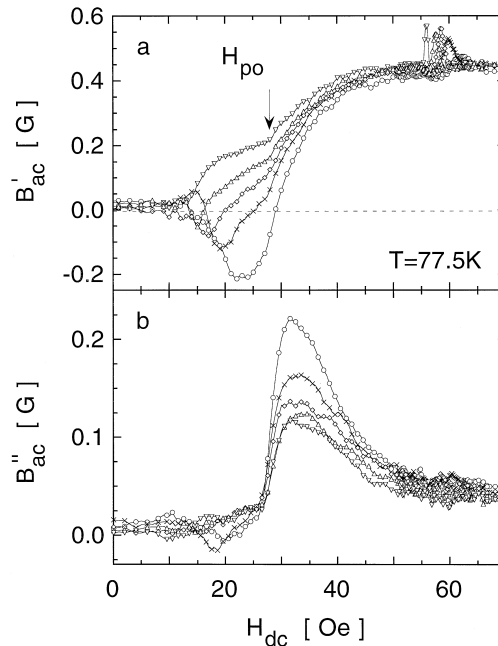


Fig. 7. Experimental B'_{ac} (a) and B''_{ac} (b) measured in BSCCO platelet using $3\ \mu\text{m}$ sensors at $T = 77.5\ \text{K}$ and $H_{ac} = 0.5\ \text{G rms}$ at various locations x/W : ∇ , 0.1, \triangle , 0.4, \diamond , 0.5, \times , 0.6, \circ , 0.9. The structure in the data at 60 Oe is due to the vortex lattice melting transition.

decreasing H_{dc} than on increasing field [31]. Note that in global measurements, the total χ' displays almost no hysteresis since trajectories 1 and 2 in Fig. 3 have very similar slopes.

Two additional and final points with regard to the platelet sample should be noted: (i) the displacement of vortices inside the droplet (Fig. 4) and within the edge region should in general result in dissipation and this is indeed observed experimentally (the finite values of B''_{ac} at $H_{dc} < H_{po}$ in Fig. 7(b)). This dissipation may become significant at high frequencies, but is small at lower frequencies, and was ignored in our calculations. (ii) The sharp peak feature at about 60 G in Fig. 7(a) is associated with the first-order vortex lattice phase transition [50] and we do not concern ourselves further with it in this manuscript.

4. Prism geometry

In the previous sections we have discussed the geometrical barrier in platelet geometry. We now turn to the effects of BL surface barrier. The BL surface barrier is present in platelet-shaped samples in addition to the geometrical barrier. In Ref. [35] a careful analysis of the global ac response for platelet samples was performed. It was shown, that geometrical and surface barriers result in very similar behavior of the ac susceptibility with only minor differences in quantitative factors (for example the position of the maximum in χ'' occurs at $H_{ac} = H_p^2/2H_{dc}$ for surface barrier and at $H_{ac} = H_p H_{c1}/2H_{dc}$ for the geometrical barrier respectively). In the platelet geometry the BL surface barrier effectively enhances the effect of the geometrical barrier without altering the qualitative local and global features. This means that it is difficult to separate the two contributions in platelet geometry without relying on specific models of the different temperature or frequency dependencies of these two barriers. We now show, however, that by changing the sample geometry the BL surface barrier can be investigated independently.

4.1. Equilibrium magnetization

Let us consider a thin long triangular prism-shaped sample of width $2W$, height d and base angle $\alpha = \arctan(d/W)$ in applied field H_a along the c -axis. As before we neglect bulk pinning, limiting our consideration to elevated temperatures. The geometrical barrier is absent in this geometry [39]. We first analyze the equilibrium magnetization process in the prism sample in the absence of a BL surface barrier. Fig. 8 shows a

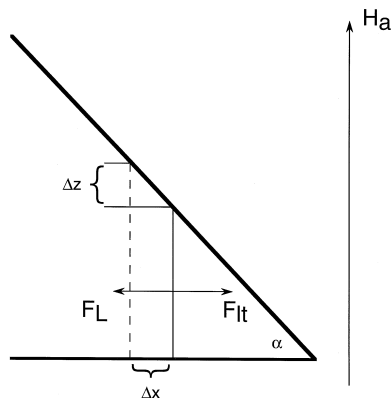


Fig. 8. Force balance of a vortex in a prism sample. The change in the potential energy due to the elongation of the vortex line with its displacement results in a force F_{lt} which acts to drive the vortex out of the sample. In the steady state situation this force is balanced by the Lorentz force F_L of the equilibrium shielding current acting towards the sample center.

simplified picture of a vortex in the prism¹. Following the same approach as developed for the edge region of the platelet sample (see Fig. 2), there are two main forces acting on the vortex. The vortex line tension ϵ_0 results in a force $F_{lt} = -dU/dx = \epsilon_0 \tan \alpha$ which drives the vortex towards the edge. In a steady state situation this force has to be balanced by the Lorentz force F_L of the shielding current, $F_L = J_e \phi_0/c$, which drives the vortex towards the center. Here J_e is the equilibrium shielding current expressed in units of the sheet current per unit width. It is interesting to note that this current flows predominantly on the top slanted surfaces of the prism, but in the following analysis only the integrated values over the sample thickness are of importance. As the applied field is increased vortices penetrate through the prism edges up to $|x| = a$. In the flux penetrated region $a < |x| < W$ the force balance $F_{lt} = F_L$ has to be maintained in steady state in a uniform equilibrium current $J_e = (c\epsilon_0/\phi_0)\tan \alpha = (cH_{c1}/4\pi)\tan \alpha$. In the vortex free region $|x| < a$ an appropriate current distribution $J_y(x)$ has to be found which results in $B_z(x) = 0$. This problem is mathematically similar to the flux penetration into a platelet sample with strong uniform bulk pinning on increasing field [51–53]. In both cases we require a uniform current in the field penetrated regions, and zero field in the flux free central region. The physical origin, however, is fundamentally different. In the strong pinning case the current acts against the pinning force expressed by the critical current J_c . This current flows in opposite direction on increasing and decreasing field resulting in hysteretic magnetization. In our case, in contrast, the current is due to the vortex line tension which acts in the same direction on both increasing and decreasing applied field, thus resulting in a fully reversible magnetization. Thus the equilibrium field and current distributions in a thin prism-shaped sample without bulk pinning are mathematically similar to a platelet strip with strong pinning on increasing applied field.

Following the notation of Ref. [51] the width of central field-free region is given by $2a$, where

$$a = \frac{W}{\cosh(H_a/B_f)} \quad (6)$$

and the characteristic field B_f is

$$B_f = \frac{4}{c} J_e. \quad (7)$$

The distribution of the sheet current $J_y(x) = J_e f(x, a)$ is expressed by

$$J_y(x) = \begin{cases} J_e, & -W < x \leq -a \\ -\frac{2J_e}{\pi} \arctan\left(\frac{x}{W} \sqrt{\frac{W^2 - a^2}{a^2 - x^2}}\right), & -a < x < a \\ -J_e, & a \leq x < W \end{cases} \quad (8)$$

and the magnetic field $B_z(x) = B_f g(x, a)$ by

$$B_z(x) = \begin{cases} 0, & -a < x < a \\ B_f \ln \frac{|x| \sqrt{W^2 - a^2} + W \sqrt{x^2 - a^2}}{a \sqrt{|x^2 - W^2|}}, & |x| \geq a \end{cases} \quad (9)$$

Note that here J_e denotes sheet current and hence should be compared with dJ_c in Ref. [51] where J_c is the critical current density and d is the sample thickness.

¹ For simplicity a straight vortex line is analyzed here. In practice the vortex is slightly curved as shown in Fig. 2. Due to the extremely high anisotropy of BSCCO, the line energy of the extra in-plane segments is negligible. Therefore it is only the extent of the vortex along the c -axis which needs to be considered for our approximate force balance evaluation.

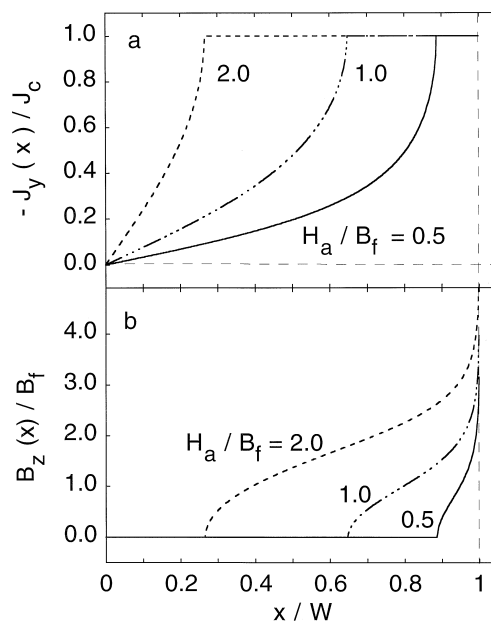


Fig. 9. Calculated current $J_y(x)$ (a) and field $B_z(x)$ (b) distributions in the prism sample under equilibrium magnetization conditions at various values of H_a following Eqs. (8) and (9). $B_z(x)$ diverges in the vicinity of the sample edge.

The corresponding distributions of $J_y(x)$ and $B_z(x)$ are presented in Fig. 9. It is important to realize that these are the equilibrium magnetization distributions which are fully reversible and result from the specific prism shape of the sample. In a thin slab with elliptical cross section for comparison, the field distribution is uniform across the sample and the sheet current is zero at $x = 0$, increasing towards the edge as $x/\sqrt{W^2 - x^2}$. Elliptical cross section is exactly the marginal case. Cross sections which are more “tapered” than an ellipse behave reversibly, and have a minimum $B_z(x)$ in the center of the sample, as in Fig. 9. In contrast, samples which are flatter than an ellipse have a maximum of $B_z(x)$ in the center (like in Fig. 4), and display hysteretic magnetization due to the presence of the geometrical barrier.

4.2. Distributed surface barrier

The BL surface barrier is usually thought to act on a vortex in close vicinity to a smooth parallel surface. It was suggested that sharp corners suppress the surface barriers in HTSC [37,38] since vortices can easily penetrate the sharp edges and then expand with no potential barrier. In the following we show that for layered HTSC systems like BSCCO, this assumption may not be relevant.

In the standard description of the BL surface barrier a straight vortex is considered in close vicinity to a parallel surface [6–8,13,14]. Once the vortex overcomes the barrier its motion within the bulk of the material is determined by the bulk properties of the sample. Let us consider a 3D vortex in a prism sample as shown in Fig. 8. In the absence of bulk pinning this vortex can be displaced reversibly as described above, and no surface barriers are involved in this process. The surface barrier is present only at the sharp edge of the prism which governs vortex entry and exit. In this case the effect of the BL surface barrier is indeed expected to be suppressed since the sharp edge acts as a weak “entry point” for the vortex and the subsequent motion of the vortex into the sample does not involve any activation process. However, in highly anisotropic layered materials like BSCCO the situation is fundamentally different. The vortex line can be considered as a stack of vortex

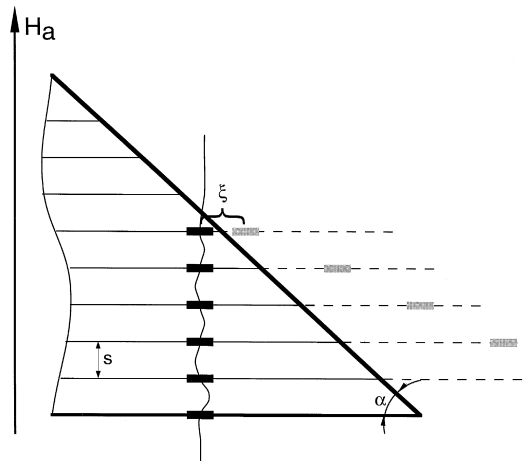


Fig. 10. The distributed BL surface barrier in a layered prism-shaped sample. The vortex line consists of a stack of pancake vortices. The interlayer distance is denoted by s . The pancake vortices interact with their images outside the slanted sample surface resulting in a local surface barrier at distances of the order of the coherence length ξ . Displacement of the vortex line towards the prism center requires addition of pancake vortices at the top of the stack. Addition of each pancake involves activation over the local surface barrier.

pancakes as shown in Fig. 10. The discrete nature of this structure results in the appearance of enhanced surface barrier effect. Here, an inward displacement of the vortex, due to a small increase of the applied field for example, results in a change of the vortex length and hence requires addition of extra vortex pancakes at the top of the stack. Each addition of a pancake involves a single local penetration event over a BL surface barrier. As a result, for any chosen location across the prism, vortex motion involves activation over the BL surface barrier. This situation is very different from the usual concept of the BL surface barrier which influences only the entry and exit processes, while the bulk vortex properties are unaffected. Here in contrast, the discrete nature of the system results in an effective barrier for vortex motion throughout the sample rather than only at the entry and exit points. Hereafter we refer to this special situation as a “distributed surface barrier”.

An alternative way of visualizing the distributed surface barrier is by noting that in the 3D case of Fig. 8 the vortex line has to “climb” a smooth potential on moving deeper into the prism. The potential increase is precisely balanced by the Lorentz force due to the equilibrium shielding current which results in fully reversible behavior as described in the previous section. In a layered system of Fig. 10, in contrast, the vortex line effectively has to “climb” a staircase corresponding to the individual layers. The average slope of the staircase is still balanced by the equilibrium shielding current. However, any advance to the next step involves an activation process over a local surface barrier. This barrier exists at any location of the vortex across the prism sample in contrast to the usual case where the surface barrier exists only at the entry point.

We emphasize that a presence of an in-plane field component does not alter the described process since the motion of a slightly tilted vortex also requires addition or removal of discrete pancakes. In addition, it is important to note that in contrast to the usual case [13] the distributed barrier is rather robust against local surface imperfections since any further advance of a vortex into the bulk beyond the defect region is impeded by the rest of the undamaged surface. It is also important to appreciate that the BL surface barrier is in fact partially distributed even in the platelet, with the “distribution” occurring over the edge region as seen in Fig. 2. The curved vortices penetrating through the sharp corners have to “acquire” additional pancakes at the edges until they reach their full length. Therefore in the highly anisotropic HTSC the sharp corners do not eliminate the BL barriers in any geometry.

The mechanism of the distributed surface barrier introduced above can be described on a microscopic level and will be presented in detail elsewhere [40]. Here we use a simple phenomenological approach in order to

model the hysteretic response due to this barrier. We thus modify the equilibrium magnetization process described in Eqs. (8) and (9) as following. On increasing applied field an additional shielding current J_{sb} has to flow in order to allow the penetrating pancake vortices to overcome the surface barrier, thus $J^{up} = J_e + J_{sb}(H_{dc})$. J_{sb} is in general field dependent [7,13,14] and decreases with increasing field. On decreasing applied field the barrier for pancake exit is very low and is neglected for simplicity, thus $J^{down} = J_e$, and only the equilibrium current due to vortex line tension is present as described in the previous section. The hysteretic dc magnetization behavior can thus be calculated using Eqs. (6)–(9) with appropriate J^{up} and J^{down} currents.

4.3. The local response for a prism-shaped sample

Now we consider the local response in a prism-shaped sample with the distributed surface barrier. The applied field is given as previously by $H_a(t) = H_{dc} + H_{ac}\cos(\omega t)$ where H_{ac} is the amplitude of the ac modulation. We calculate the local ac response B'_{ac} and B''_{ac} in the same way as we did for the case for the platelet-shaped sample. We again consider the quasistatic limit and use Eqs. (6)–(9) above replacing J_e by $J^{up} = J_e + J_{sb}$ on increasing applied field and $J^{down} = J_e$ on decreasing field. For simplicity we assume a linear decrease of the surface barrier current with the applied field, $J_{sb} \propto H_{ir} - H_{dc}$ for $H_{dc} \leq H_{ir}$, and $J_{sb} = 0$ at fields above the irreversibility field H_{ir} where the surface barrier vanishes.

At $t = 0$ the instantaneous applied field is at its maximum value $H_{max} = H_{dc} + H_{ac}$. At this point the width of the flux-free region attains its lowest value $a_0 = a(H_{max}, J^{up})$ described by Eqs. (6) and (7) with current J^{up} and corresponding characteristic field B_f^{up} . The current and field distributions are shown by $\theta = \omega t = 0^\circ$ curves in Fig. 11. As the field decreases vortices near the prism edges leave the sample. In order to describe this process we use a superposition method following Ref. [51], with two terms. The first term is the distribution at H_{max} described by Eqs. (6)–(9) with J^{up} . This is our initial state. The second term describes the change with

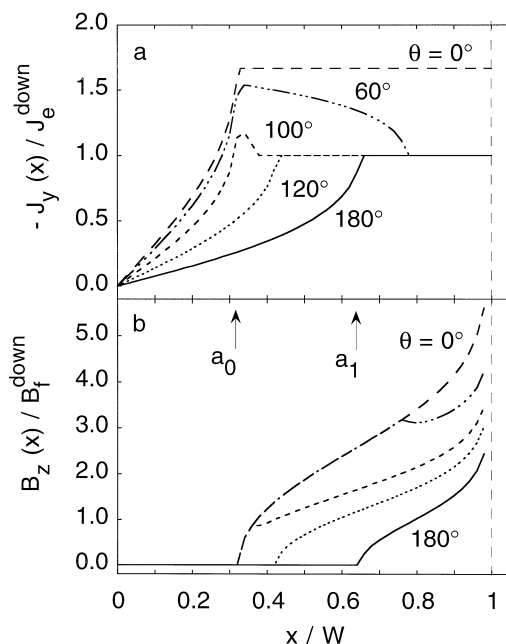


Fig. 11. Calculated profiles of $J_y(x)$ (a) and $B_z(x)$ (b) for decreasing instantaneous applied field in the prism sample with distributed surface barrier at different phase, θ , of the ac field ($\theta = \omega t$). $\theta = 0^\circ$ corresponds to the initial state, $H_{max} = H_{dc} + H_{ac}$, and $\theta = 180^\circ$ corresponds to $H_{min} = H_{dc} - H_{ac}$ ($H_{dc} = 2B_f^{down}$, $H_{ac} = B_f^{down}$, $J_{sb}(H_{dc})/J_e = 0.66$).

respect to the H_{\max} state. It is given by the same equations but with parameter $a = a(H_{\max} - H_a, J_{\text{sb}})$ and with a current $J^{\text{down}} - J^{\text{up}} = -J_{\text{sb}}$ which flows in the opposite direction. As a result at $x > a$ the total current is $J^{\text{down}} = J_e$ which allows vortex exit near the edges. This situation is depicted for example by the $\theta = 60^\circ$ curve in Fig. 11. We emphasize that in the prism geometry with no bulk pinning the current always flows in the same direction and the field is positive everywhere. This is in contrast to the platelet case with strong bulk pinning where a negative current is flowing in the outer region when the field is decreased. This negative current also results in a negative field at the edges (see for example Fig. 5 in Ref. [51]) and as a result antivortices are present at the edges. These annihilate the pinned vortices as the field is decreased. In Fig. 11, however, no antivortices are present provided that $H_a \geq 0$. In the outer region the current is the equilibrium current J_e which results in zero net force and the vortices may leave the sample. At $a_0 < x < a$, however, $J_e < J < J_e + J_{\text{sb}}$ and the vortices are “frozen” resulting in invariant $B_z(x)$ distribution in this region (Fig. 11(b)). Here the vortices cannot move deeper into the sample since the Lorentz force is not sufficient to overcome the pancake surface barrier. On the other hand, they cannot move outward since this force is larger than the outward line tension force. So the larger current holds the vortices against the distributed surface barrier. This situation is similar to the bulk pinning case with $-J_e < J < J_e$ where vortices are immobile.

As field is further decreased a decreases and more vortices leave the sample. If H_{ac} is sufficiently large, as is the case shown in Fig. 11, a will reach a_0 at which point $J \leq J_e$ everywhere and all the previous magnetization history is erased. At lower fields the field free region expands and $J_y(x)$ and $B_z(x)$ are described by the equilibrium magnetization Eqs. (6)–(9) with $a = a(H_a, J_e)$ (see $\theta = 120^\circ$ and 180° curves in Fig. 11).

In order to calculate the response during the increasing half wave of the ac field we take the distribution at $\theta = 180^\circ$ as the new initial state. If H_{ac} is sufficiently large this state is described by one parameter $a_1 = a(H_{\text{min}}, J_e)$, as is the case in Figs. 11 and 12. For low ac amplitudes, however, this state is represented by the superposition of two distributions described by a_0 and a_1 . As field is increased the profiles are given by superposition of the initial state at H_{min} and the new additional distribution described by Eqs. (6)–(9) with

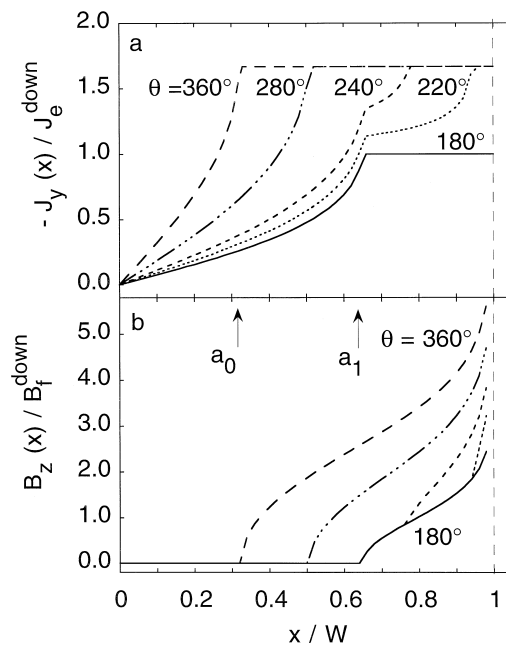


Fig. 12. Calculated current (a) and field (b) profiles as in Fig. 11 for increasing instantaneous applied field in the prism at different phase θ of ac field. $\theta = 180^\circ$ corresponds to H_{min} and $\theta = 360^\circ$ corresponds to H_{max} .

$a = a(H_a - H_{\min}, J_{\text{sb}})$ with a current $J^{\text{up}} - J^{\text{down}} = J_{\text{sb}}$ which flows in the positive direction. At $x > a$ the total current is therefore $J^{\text{up}} = J_c + J_{\text{sb}}$ allowing new vortices to penetrate into the edges as shown for $\theta = 220^\circ$ and 240° in Fig. 12. This solution holds until a reaches a_1 at which point the previous history at H_{\min} is erased and the profiles are described by one parameter $a = a(H_a, J^{\text{up}})$, as shown in Fig. 12 for $\theta = 280^\circ$ and 360° . From the above analysis we can construct $B_z(x, t)$ for the entire ac period at any location across the sample.

4.4. Numerical simulations and experimental results

The local ac response is a Fourier transform of instantaneous $B_z(t)$. Figs. 13 and 14 show the calculated ac response $B'_{\text{ac}} - iB''_{\text{ac}}$ at different locations across the sample as a function of H_{dc} at high and low amplitudes of H_{ac} respectively. At relatively large H_{ac} the width of flux-free region in the center of the prism modulates with the instantaneous ac field as shown in Figs. 11 and 12. At the flux front the rise of $B_z(x)$ is very steep resulting in a sharp peak in the local B'_{ac} as seen in Fig. 13(a). The flux front moves deeper into the sample as H_{dc} increases. Qualitatively similar behavior is observed experimentally as shown in Fig. 15. The sharp peaks are smeared out in experiment due to the averaging over the finite area of the Hall sensor. In addition the steep flux front at $x = a$ which is obtained theoretically for infinitely thin sample is in practice smoothed over a width of the order of the samples thickness. The out-of-phase component B''_{ac} shows a sharp dissipation peak that occurs closer to the prism center as H_{dc} is increased. Interestingly, the maximum value of B''_{ac} is obtained at $x \approx 0.6$ both theoretically, Fig. 13(b), and experimentally, Fig. 15(b). The exact shape of the response as a function of H_{dc} depends on how the surface barrier decreases with the field. In our analysis we have assumed the simplest linear decrease to zero at H_{ir} . This simple form gives a satisfactory qualitative description of the observed response.

A further important observation is that B''_{ac} obtains negative values at higher values of H_{dc} near the edges as

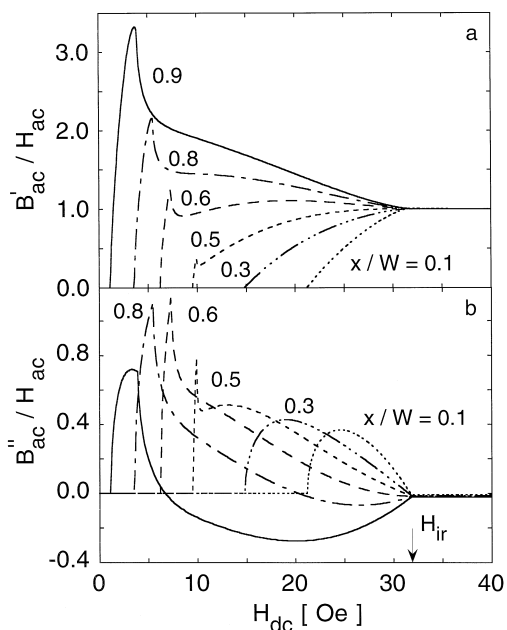


Fig. 13. Calculated ac response B'_{ac} (a) and B''_{ac} (b) for the prism sample as a function of H_{dc} for a large ac field $H_{\text{ac}} = 2$ G rms, $B_f^{\text{down}} = 4$ G, $B_f^{\text{up}}(0) = 8$ G, $H_{\text{ir}} = 32$ G for different locations across the crystal. Sharp peaks of B'_{ac} are obtained due to modulation of the width of the vortex-filled region. The maximum of dissipation signal B''_{ac} occurs at $x/W \approx 0.6$. B''_{ac} near the sample edge attains negative values at large H_{dc} .

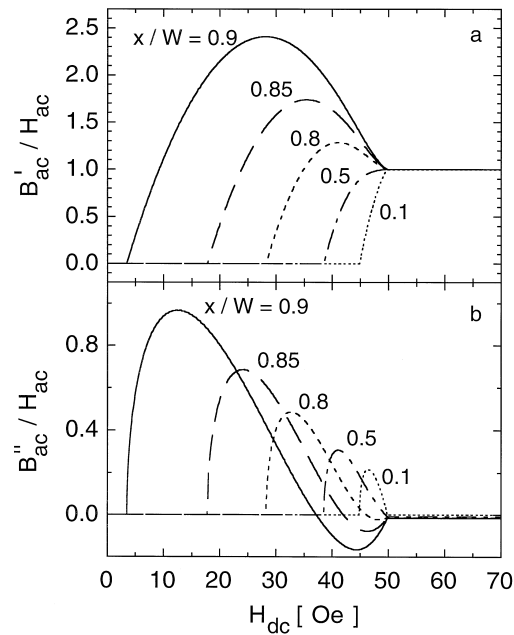


Fig. 14. Calculated ac responses B'_{ac} (a) and B''_{ac} (b) similar to Fig. 13 but for a low ac field $H_{ac} = 0.4$ G rms, $B_f^{down} = 4$ G, $B_f^{up}(0) = 8$ G, $H_{ir} = 50$ G. Both B'_{ac} and B''_{ac} change gradually with H_{dc} . Maximum of dissipation takes place near the sample edge.

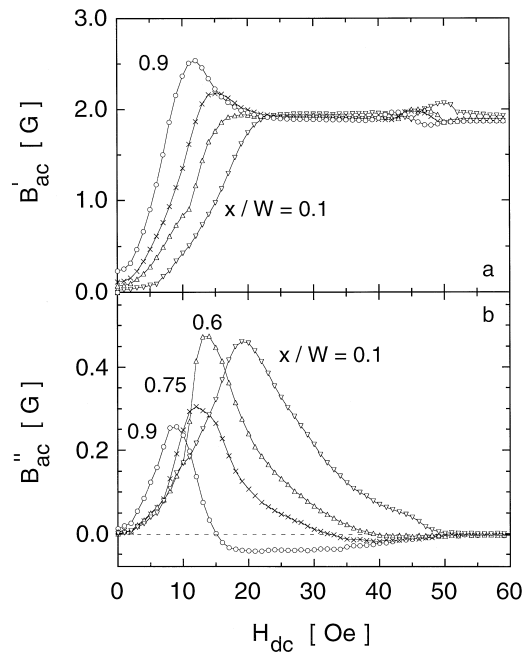


Fig. 15. Experimental ac response B'_{ac} (a) and B''_{ac} (b) in the prism BSCCO sample ($T = 85$ K) as a function of H_{dc} for a large ac field $H_{ac} = 2$ G rms at different locations across the sample x/W : ∇ , 0.1, \triangle , 0.6, \times , 0.75, \circ , 0.9. The structure in B'_{ac} at about 50 Oe is due to the vortex lattice melting transition.

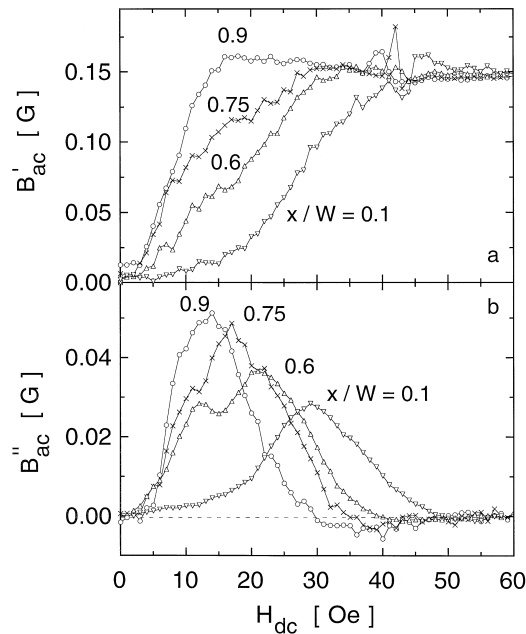


Fig. 16. Experimental ac response B'_{ac} (a) and B''_{ac} (b) in the BSCCO prism sample at different locations across the sample as in Fig. 15 but at a low ac field $H_{ac} = 0.15$ G rms.

shown both theoretically and experimentally in Figs. 13 and 15. The origin of this behavior is as follows. The change in local field away from the edge of the sample is delayed with respect to the modulation of the applied field (defined as positive B'_{ac} in Figs. 13 and 15) because the perturbation of the external field must first propagate to the observation point. Remarkably, at large H_{dc} , the change of internal field near the edge of the sample is sufficiently rapid (because of the divergence of $B_z(x)$ at $x \approx W$) that the resulting first harmonic of the ac response precedes the ac applied field and the sign of the observed B''_{ac} is inverted.

Fig. 14 describes the ac response at low H_{ac} . In this case the position of the flux front is determined by H_{dc} and the position of the front does not oscillate during the ac cycle. The vortices enter and leave the sample near the edge and central part is effectively shielded from the ac signal. As H_{dc} is increased the surface barrier is monotonically suppressed and the ac signal penetrates deeper into the sample until a fully reversible behavior is obtained at $H_{dc} \geq H_{ir}$. As a result a rather smooth dependence of B'_{ac} on H_{dc} is obtained as shown in Fig. 14(a)Fig. 16(a). The out-of-phase component also displays smooth behavior. In this case the largest B''_{ac} is obtained near the edge of the prism as shown theoretically (Fig. 14(b)) and verified experimentally (Fig. 16(b)). This is in marked contrast to the behavior at large H_{ac} which is shown in Figs. 13 and 15.

5. Conclusions

There are numerous important differences between the local ac response of platelet- and prism-shaped samples in the absence of bulk pinning which can be summarized as following. (i) The in-phase response B'_{ac} in a platelet sample (Fig. 7(a)) is always largest in the center, whereas in a prism (Fig. 15(a)Fig. 16(a)) it is always smallest in the center. (ii) In a prism the ac signal penetrates gradually from the edges starting from almost zero H_{dc} , whereas in a platelet the ac signal is fully screened until a well defined dc penetration field. (iii) In the platelet, a negative B'_{ac} is obtained while it is always positive in the case of the prism. These differences arise

from the fact that in the prism a vortex-free region in the center of the sample is surrounded by vortex-filled regions near the edges (Fig. 9). The vortex-filled regions *expand* in phase with the external ac field. In the platelet the situation is just the opposite. The vortex-filled region is in the center of the sample and it is surrounded by vortex-free regions. This central vortex-filled region *shrinks* as the instantaneous field rises in contrast to prism. (iv) The B''_{ac} also shows major differences in the H_{dc} dependencies in prism- and platelet-shaped crystals. In the prism the dissipation peak occurs first near the sample edges and moves inward as H_{dc} is increased (Fig. 15(b) Fig. 16(b)). In the platelet, in contrast, the dissipation peak occurs simultaneously at all locations (Fig. 7(b)). (v) In the prism B''_{ac} shows broad features and finite dissipation within the sample is present at all fields below H_{ir} . In the platelet however, the dissipation appears abruptly and is present only in a relatively narrow range at elevated H_{dc} . (vi) A sharp onset of B''_{ac} is always obtained at the edges of the platelet sample. In the prism, however, the relative height of the dissipation peaks depends on the amplitude of the ac field (Fig. 15(b) Fig. 16(b)). (vii) In addition, B''_{ac} attains negative values in the prism, while it is always positive in the platelet. These fundamental differences in the dissipation mechanisms arise from the fact that in a platelet the geometrical and surface barriers are concentrated at the sample edges, whereas in a prism the surface barriers are distributed over the entire width of the sample. As a result any displacement of vortices in the prism is accompanied by dissipation and hence B''_{ac} is present at any $H_{dc} < H_{ir}$. In the platelet, vortex displacement in the bulk causes negligible dissipation. Significant dissipation arises in this sample only when vortices have to cross the edges and overcome the barriers during the ac cycle. This occurs only in a relatively narrow range $H_{po} < H_{dc} < H_{ir}$, with a peak in dissipation that is detected simultaneously at all locations across the sample.

In summary, we have observed major differences in the ac response of samples with different shapes which emphasize the dominant role of surface and geometrical barriers in BSCCO crystals at elevated temperatures. Bulk pinning, in contrast, results in a very different response, the qualitative behavior of which is insensitive to the specific shape of the sample. We have developed a simple model to describe the effects of a distributed surface barrier and of the resulting local ac response in a prism-shaped sample. The model provides both qualitative and quantitative description of the ac response in agreement with experimental data.

Acknowledgements

We thank H. Motohira for providing the BSCCO crystals, H. Shtrikman for growing the GaAs heterostructures, and D. Majer for Hall probe fabrication. Elucidating discussions with L. Burlachkov, V. Vinokur, and A. Koshelev are gratefully acknowledged. This research was supported by German–Israeli Foundation for Scientific Research and Development (GIF), US–Israel Binational Science Foundation (BSF), by MINERVA Foundation, Munich, Germany, and by Alhadeff Research Award.

References

- [1] For a recent review see G. Blatter, M.V. Feigelman, V.B. Geshkenbein, A.I. Larkin, V.M. Vinokur, Rev. Mod. Phys. 66 (1994) 1125.
- [2] For a recent review see E.H. Brandt, Rep. Prog. Phys. 58 (1995) 1465.
- [3] Y. Yeshurun, A.P. Malozemoff, A. Shaulov, Rev. Mod. Phys. 68 (1996) 911.
- [4] C.P. Bean, Rev. Mod. Phys. 36 (1964) 31.
- [5] A.M. Campbell, J.E. Evetts, Adv. Phys. 21 (1972) 199.
- [6] C.P. Bean, J.D. Livingston, Phys. Rev. Lett. 12 (1964) 14.
- [7] J.R. Clem, in: K.D. Timmerhaus, W.J. O'Sullivan, E.F. Hammel (Eds.), Proceedings of the 13th Conference on Low Temperature Physics (LT13), vol. 3, Plenum, New York, 1974, p. 102.
- [8] V.N. Kopylov, A.F. Koshelev, I.F. Schegolev, T.G. Togonidze, Physica C 170 (1990) 291.
- [9] M. Konczykowski, L.I. Burlachkov, Y. Yeshurun, F. Holtzberg, Phys. Rev. B 43 (1991) 13707.
- [10] M. Konczykowski, L.I. Burlachkov, Y. Yeshurun, F. Holtzberg, Physica C 194 (1992) 155.
- [11] M. Konczykowski, Progress in High Temperature Superconductivity, vol. 30, World Scientific, Singapore, 1992, p. 152.

- [12] N. Chikomoto, M. Konczykowski, N. Motohira, A.P. Malozemoff, *Phys. Rev. Lett.* 69 (1992) 1260.
- [13] L. Burlachkov, *Phys. Rev. B* 47 (1993) 8056.
- [14] L. Burlachkov, V.B. Geshkenbein, A.F. Koshelev, A.I. Larkin, V.M. Vinokur, *Phys. Rev. B* 50 (1994) 16770.
- [15] X. Xu et al., *Phys. Rev. B* 48 (1993) 10630.
- [16] Y.C. Kim et al., *Phys. Rev. B* 52 (1995) 4438.
- [17] R.B. Flippen et al., *Phys. Rev. B* 52 (1995) R9828.
- [18] E. Zeldov et al., *Phys. Rev. Lett.* 73 (1994) 1428.
- [19] E. Zeldov et al., *Physica C* 235–240 (1994) 2761.
- [20] T.B. Doyle, PhD Thesis, Univ. of Witwatersrand (1975).
- [21] R. Labusch, T.B. Doyle, in: K. Tachikawa et al. (Eds.), *Proc. Int. Cryogenic Materials Conf. Critical State in Superconductors*, Honolulu, Hawaii, 1994, World Scientific, Singapore, 1995, p. 206.
- [22] T.B. Doyle, R. Labusch, *J. Low Temp. Phys* 105 (1996) 1207.
- [23] M.V. Indenbom, H. Kronmuller, T.W. Li, P.H. Kes, A.A. Menovsky, *Physica C* 222 (1994) 203.
- [24] M.V. Indenbom, H. Kronmuller, T.W. Li, P.H. Kes, A.A. Menovsky, *Physica C* 235–240 (1994) 201.
- [25] Th. Schuster, M.V. Indenbom, H. Kuhn, E.H. Brandt, M. Konczykowski, *Phys. Rev. Lett.* 73 (1994) 1424.
- [26] B. Khaykovich et al., *Physica C* 235–240 (1994) 2757.
- [27] I.L. Maximov, A.A. Elistratov, *JETP Lett.* 61 (1995) 208.
- [28] E. Zeldov et al., *Europhys. Lett.* 30 (1995) 367.
- [29] D. Majer et al., in: G. Deutscher, A. Revcolevschi (Eds.), *Coherence in High- T_c Superconductors*, World Scientific (Singapore), 1996, p. 271.
- [30] M. Marchevsky, L.A. Gurevich, P.H. Kes, J. Aarts, *Phys. Rev. Lett.* 75 (1995) 2400.
- [31] N. Morozov, E. Zeldov, D. Majer, B. Khaykovich, *Phys. Rev. Lett.* 76 (1996) 138.
- [32] M. Benkraouda, J.R. Clem, *Phys. Rev. B* 53 (1996) 5716.
- [33] M. Wurlitzer et al., *Z. Physik B* 101 (1996) 561.
- [34] R.I. Khasanov, Yu.I. Talanov, Yu.M. Vashakidze, G.B. Teitel'baum, *Physica C* 242 (1995) 333.
- [35] C.J. van der Beek, M.V. Indenbom, G. D'Anna, W. Benoit, *Physica C* 258 (1996) 105.
- [36] T.B. Doyle et al., unpublished.
- [37] M.V. Indenbom, E.H. Brandt, *Phys. Rev. Lett.* 73 (1994) 1731.
- [38] M.V. Indenbom et al., *Proc. of the 7th Int. Workshop on Critical Currents in Superconductors*, Alpbach, World Pub. Co., 1994, p. 327.
- [39] D. Majer, E. Zeldov, M. Konczykowski, *Phys. Rev. Lett.* 75 (1995) 1166.
- [40] L. Burlachkov et al., unpublished.
- [41] N. Motohira et al., *J. Ceram. Soc. Jpn. Int. Ed.* 97 (1989) 994.
- [42] J.R. Clem, *J. Appl. Phys.* 50 (1979) 3518.
- [43] E.H. Brandt, *Phys. Rev. Lett.* 67 (1991) 2219.
- [44] E.H. Brandt, *Phys. Rev. Lett.* 68 (1992) 3769.
- [45] E.H. Brandt, *Phys. Rev. Lett.* 71 (1993) 2821.
- [46] E.H. Brandt, *Phys. Rev. B* 49 (1994) 9024.
- [47] V.B. Geshkenbein, V.M. Vinokur, R. Fehrenbacher, *Phys. Rev. B* 43 (1991) 3748.
- [48] J.R. Clem, A. Sanchez, *Phys. Rev. B* 50 (1994) 9355.
- [49] M.A. Skvortsov, V.B. Geshkenbein, *Zh. Eksp. Teor. Fiz.* 105 (1994) 1379 [*Sov. Phys. JETP* 78 (1994) 743].
- [50] N. Morozov, E. Zeldov, D. Majer, M. Konczykowski, *Phys. Rev. B* 54 (1996) R3784.
- [51] E. Zeldov, J.R. Clem, M. McElfresh, M. Darwin, *Phys. Rev. B* 49 (1994) 9802.
- [52] E.H. Brandt, M.V. Indenbom, *Phys. Rev. B* 48 (1993) 12893.
- [53] E.H. Brandt, M.V. Indenbom, A. Forkl, *Europhys. Lett* 22 (1993) 735.